PHOTONICS Research

Frequency upconversion detection of rotational Doppler effect

Haoxu Guo,[1] Xiaodong Qiu,[1,3] Song Qiu,[2] Ling Hong,[1] Fei Lin,[1] Yuan Ren,[2,4] and Lixiang Chen[1,5]

[1]Department of Physics and Collaborative Innovation Center for Optoelectronic Semiconductors and Efficient Devices, Xiamen University, Xiamen 361005, China
[2]Department of Aerospace Science and Technology, Space Engineering University, Beijing 101416, China
[3]e-mail: qxd@xmu.edu.cn
[4]e-mail: renyuan_823@aliyun.com
[5]e-mail: chenlx@xmu.edu.cn

Received 31 August 2021; revised 16 November 2021; accepted 16 November 2021; posted 16 November 2021 (Doc. ID 441785); published 21 December 2021

We demonstrated an efficient scheme of measuring the angular velocity of a rotating object with the detection light working at the infrared regime. Our method benefits from the combination of second-harmonic generation (SHG) and rotational Doppler effect, i.e., frequency upconversion detection of rotational Doppler effect. In our experiment, we use one infrared light as the fundamental wave (FW) to probe the rotating objects while preparing the other FW to carry the desired superpositions of orbital angular momentum. Then these two FWs are mixed collinearly in a potassium titanyl phosphate crystal via type II phase matching, which produces the visible second-harmonic light wave. The experimental results show that both the angular velocity and geometric symmetry of rotating objects can be identified from the detected frequency-shift signals at the photon-count level. Our scheme will find potential applications in infrared monitoring.

https://doi.org/10.1364/PRJ.441785

1. INTRODUCTION

The linear Doppler effect describes a phenomenon that electromagnetic waves or sound waves reflected from a moving object will cause a frequency shift, which has been extensively utilized to measure the linear velocity of an object [1]. Analogously, when light is reflected or emitted from a rotating object, it will undergo a frequency shift, which is the rotational version of Doppler effect [2]. The rotational Doppler effect, associated with photon spin angular momentum, was originally observed and analyzed by Garetz *et al.*, who used rotating half-wave plates (HWPs) of angular velocity to imprint a frequency shift to circularly polarized light [3]. Subsequently, the rotational Doppler effect was also manifested by using millimeter waves, in which the amount of rotational Doppler shift is related to the orbital angular momentum (OAM) [4,5]. It was Lavery and coworkers that demonstrated the rotational Doppler effect in the visible light region, which enabled the measurement of angular velocity with the light beam scattered from the rough surface of a spinning object [6]. From the applied point of view, the rotational Doppler effect has seen a wide range of applications for angle remote sensing, from the microscopic world to the aerospace field [7]. Through the coherent interaction between OAM beams and rubidium atoms at room temperature, Barreiro *et al.* reported on the first spectroscopic observation of rotational Doppler shift [8]. Luo *et al.* theoretically predicted that when an OAM beam interacts with a left-handed material, the rotational Doppler effect will induce a transfer of angular momentum from the material to the beam [9]. Korech *et al.* demonstrated a new method to control and detect the spinning molecule microscopically based on the rotational Doppler effect [10]. Zhou *et al.* demonstrated the optical rotational Doppler effect via theoretical analysis and experimental verification, and they developed the OAM complex spectrum analyzer based on this effect [11,12]. In a city environment, we built a 120 m free-space link between the rooftops of two buildings to detect the angular velocity of rotating objects from the observed rotational frequency shifts [13]. Besides, rotational Doppler effect was exploited to deduce the angular acceleration rate of a spinning object [14]. Also, Qiu *et al.* investigated the influence of the lateral misalignment and the tilted angle on the measurement of rotational Doppler effect [15,16]. Recently, we explored the quantum correlations of spatially entangled photons for angle remote sensing in a nonlocal manner [17].

It is worth noting that infrared remote sensing may be more advantageous in certain applications, such as infrared monitoring in the military realm [18], non-destructive and reagent-free biological detection [19–21], remote sensing of urban climate [22], and ocean remote sensing [23,24]. However, suffering from exorbitant prices, relatively low quantum efficiency, severe dark current, and requiring additional cryogenic cooling, the

development of infrared detection is seriously affected [25]. Moreover, it is difficult to achieve simple and efficient image detection in the mid-infrared regime with existing detector technologies [26,27]. To circumvent this constraint, ultrasensitive infrared detection can be expected with nonlinear frequency conversion from the infrared light field to the visible spectral region by leveraging the high sensitivity of visible single-photon counting modules [25,28–32]. This strategy has been demonstrated to build all-optical upconversion imaging systems for few-photon-level full two-dimensional infrared imaging [33]. Here, via second-harmonic generation (SHG), we extend this scheme to measure the rotational Doppler shifts from the infrared detected light to visible with a high-efficiency single-photon detector. Actually, a clever scheme has been devised by Li and coworkers to report the rotational Doppler effect in nonlinear optics, in which the frequency shifts were imparted by the rotating nonlinear crystal itself [34,35]. Instead, we rotate one fundamental wave (FW) by illuminating it onto a spinning object while preparing the other FW to carry the desired OAM superpositions and thus enabling the detection of frequency shifts and angular velocity of rotating objects from SHG light.

2. METHOD

The Laguerre–Gaussian (LG) modes, as one kind of typical OAM eigenmode, are conceived as a set of orthogonal and complete basis vectors in high-dimensional Hilbert space. In the cylindrical coordinate (ρ, ϕ), a standard LG mode at the beam waist plane $z = 0$ can be written as

$$\mathrm{LG}_p^{\ell}(\rho, \phi) = R_p^{\ell}(\rho) \exp(i\ell\phi) \tag{1}$$

and

$$R_p^{\ell}(\rho) = C_{p,\ell} \left(\frac{\sqrt{2}\rho}{\omega}\right)^{|\ell|} \exp\left(\frac{-\rho^2}{\omega^2}\right) L_p^{|\ell|}\left(\frac{2\rho^2}{\omega^2}\right), \tag{2}$$

where p and ℓ are the radial and azimuthal mode indices, ω is the beam waist, $C_{p,\ell}$ is the normalized constant, and $L_p^{|\ell|}(\cdot)$ is the generalized Laguerre polynomial. According to the concept of digital spiral imaging [36], we can describe the transmission function or the rough surface of any rotating object $E_1(\rho, \phi)$ in terms of LG modes, namely, $E_1(\rho, \phi) = \sum_{\ell,p} A_{\ell,p} \mathrm{LG}_p^{\ell}(\rho, \phi)$, where the complex amplitude, $A_{\ell,p} = \iint [\mathrm{LG}_p^{\ell}(\rho, \phi)]^* \cdot E_1(\rho, \phi)\rho \mathrm{d}\rho \mathrm{d}\phi$. Here we define the normalization coefficients $a_\ell = A_{\ell,p=0}/A_{\ell=0,p=0}$ for the OAM modes. For an easy visualization, we plot in Fig. 1 the OAM mode intensity spectra $|a_\ell|^2$ for three typical objects of different rotational symmetries, i.e., a three-leaf clover, a hexagonal snowflake, and a cartoon pattern. It can be observed that the principal components of LG modes are distributed over those modes with the azimuthal indices of $\ell = 0, \pm 3, \pm 6, \ldots$ for the clover in Fig. 1(a) and over $\ell = 0, \pm 6, \pm 12, \ldots$ for the snowflake in Fig. 1(b), which reveals the threefold and sixfold rotational symmetries, respectively. Another object in Fig. 1(c), the cartoon pattern, contains a variety of LG mode components ranging from $\ell = 0$ to $\ell = \pm 6$ and thus reflects its own structural property of low symmetry.

The mathematical picture of eigenmode decomposition offers us a more intuitive understanding on the physical origin

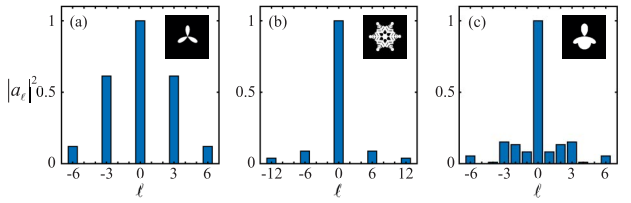

Fig. 1. OAM mode spectra ($p = 0$) for three objects of different rotational symmetries: (a) three-leaf clover, (b) hexagonal snowflake, and (c) cartoon pattern.

of rotational Doppler effect. Assume that the rotating object has a constant angular velocity Ω around its own axis; as a result, we can describe the transmission function of the object as

$$E_1(\rho, \phi) \to E_1(\rho, \phi + \Omega t) = \sum_{\ell,p} A_{\ell,p} R_p^{\ell}(\rho) \exp(i\ell\phi) \exp(i\ell\Omega t). \tag{3}$$

It can be seen clearly from Eq. (3) that, as a result of rotation, an additional time-dependent and OAM-related phase variation of $\exp(i\ell\Omega t)$ has been individually induced to each OAM component, which is just equivalent to a frequency shift of $\ell\Omega$. This result has been well known and extensively reported in the realm of linear optics [2,4–16]. However, to the best of our knowledge, only a little attention has been paid to extend the rotational Doppler effect to nonlinear optical realm [34,35]. Such an extension is crucial for realizing high-efficiency infrared detection via frequency upconversion. Instead of rotating the nonlinear crystal as in Refs. [34,35], we directly mix the infrared FW bearing the rotational Doppler signal of Eq. (3) with another FW carrying desired OAM superpositions. Then, via SHG, we can realize the transfer of rotational Doppler signals from the infrared to the visible region. Under the paraxial approximation and the slowly varying amplitude approximation, we can describe the generation of SHG light field by the following wave-coupling equation [37]:

$$\frac{\mathrm{d}E_{\mathrm{SHG}}(\rho, \phi, t)}{\mathrm{d}z} = \frac{i2\pi \mathrm{d}_{\mathrm{eff}}}{\lambda_{\mathrm{vis}} n_{\mathrm{vis}}} E_1(\rho, \phi + \Omega t) E_2(\rho, \phi), \tag{4}$$

where d_{eff} is the effective nonlinear coefficient, z is the propagation distance, and λ_{vis} and n_{vis} are the visible light wavelength and the crystal refractive index, respectively. Here we use type II phase-matching condition to do SHG, in which two FWs should be of orthogonal horizontal and vertical polarizations such that self-interaction of each FW can be well suppressed. Then, in the case of small signal approximation, the SHG light field can be simply expressed as

$$E_{\mathrm{SHG}}(\rho, \phi, t) \propto E_1(\rho, \phi + \Omega t) E_2(\rho, \phi). \tag{5}$$

In order to extract the rotational Doppler signals of the infrared light $E_1(\rho, \phi + \Omega t)$, we prepare the other FW as two specific OAM mode superpositions, namely, $E_2(\rho, \phi) = [\exp(im\phi) + \exp(-im\phi)]/\sqrt{2}$. This process is just equivalent to using an OAM filter of $\ell = \pm m$ to perform the detection of the intensity modulation frequency $f_{\mathrm{mod}} = m\Omega/\pi$ and thus infer the angular velocity Ω [6]. Unlike the linear optical case, the intensity modulation frequency f_{mod}, is measured from the

SHG light as a result of the transfer of rotational Doppler shift in the process of SHG. Besides, it is worth mentioning that the possible rotational symmetry of the detected objects can also be inferred from the measured Doppler signals, as its intensity is also determined by $|a_\ell|^2$, being related to the rotational symmetry of the object. We demonstrate these key results of frequency upconversion and symmetry-determined rotational Doppler effect in the following experimental section.

3. EXPERIMENTS

In our experimental implementation, as shown in Fig. 2, the horizontally polarized light beam derived from a near-infrared 1064 nm laser (Cobolt, Rumba) is expanded and collimated by a telescope, and then it is directed to illuminate a computer-controlled spatial light modulator (SLM, Hamamatsu, X10468-7). The SLM is divided into two regions, each of which has a pixel array of 400 × 600. We simulate the rotating objects by preparing time-varying holographic gratings in region I and display the desired OAM superpositions in region II. As the light beams reflected from these two regions are nearly collinear, we employ an additional D-shaped mirror to separate them spatially. Then, after probing the rotating objects, one infrared FW is imparted with the rotational Doppler signals $E_1(\rho, \phi + \Omega t)$, in which each OAM mode individually experiences a time-dependent phase shift of $\exp(i\ell\Omega t)$ as manifested by Eq. (3). In order to extract the angular velocity of the rotating object, we prepare the other FW in the conjugated OAM superpositions $E_2(\rho, \phi) = [\exp(im\phi) + \exp(-im\phi)]/\sqrt{2}$. Besides, as the potassium titanyl phosphate (KTP) crystal is cut for type II phase matching, we build a polarization-dependent interferometer to recombine these two FWs. For this, we insert an additional HWP with its fast axis orienting at 45° in one arm to rotate the horizontal polarization of the OAM beam into the vertical one. After a polarizing beam splitter (PBS), the recombined beam is incident on a 5 mm × 5 mm × 5 mm KTP crystal to participate in SHG process. Note that a $4f$ system consisting of two lenses ($f_1 = 750$ mm and $f_2 = 100$ mm) with an iris in each focal plane is nested to filter out the first-order diffraction, which is equivalently imaged onto the facet of KTP crystal. The visible SHG light is then obtained after a narrow filter centered at 532 nm. Thus, according to Eqs. (3) and (5), we can write the SHG light field in terms of OAM modes as

$$E_{\mathrm{SHG}}(\rho, \phi, t) \propto \sum_{\ell,p} A_{\ell,p} R_p^{\ell}(\rho) \times \{\exp[i(\ell + m)\phi] + \exp[i(\ell - m)\phi]\} \exp(i\ell\Omega t). \quad (6)$$

Subsequently, we use another $4f$ system ($f_3 = 150$ mm and $f_4 = 10$ mm) to collect and couple the SHG light into a single-mode fiber (SMF) that is connected to a single-photon counting module (SPCM). Note that SMF is acting as a zero OAM mode filter such that only those photons satisfying $\ell = \pm m$ can be detected by SPCM. In the backprojection picture, we can equivalently consider that a fundamental Gaussian mode is emitted from the SMF and then illuminates the crystal after being expanded by the $4f$ system [38]. We estimate that the beam waist of the expanded Gaussian mode is ~1.0 mm, being sufficiently larger than the spot of SHG light ~0.25 mm at the output plane of the crystal. Thus, the combination of SMF and SPCM can be regarded as a bucket detector to collect all the rotational Doppler signals. Then we know from Eq. (6) the time-dependent intensity modulation can be written as $I_m(t) \propto |a_m|^2[\cos(2m\Omega t) + 1]$. The transfer of rotational Doppler frequency shift is manifested by the OAM-dependent intensity of SHG light with a modulation frequency $f_{\mathrm{mod}} = m\Omega/\pi$ after a straightforward Fourier transform $\tilde{I}_m(f) = F\{I_m(t)\}$.

In our first set of experiments, we simulate a rotating object of three-leaf clover by using a computer-generation hologram in SLM. For the rotating clover, we set $\Omega = 1$ deg/s and 2 deg/s, respectively. For each case, we measure the rotational frequency shifts by scanning the OAM superpositions from $m = \pm 1$ to $m = \pm 6$. We illustrate in Fig. 3 the experimental results, in which Figs. 3(a) and 3(b) are the photon counts of SHG light recorded by SPCM while Figs. 3(c) and 3(d) are the power spectra of rotational Doppler signals after fast Fourier transform (FFT). In each case, the cosine oscillations of single-photon events can be seen clearly when OAM superpositions $m = \pm 3$ and $m = \pm 6$ are used. In contrast, the single-photon signals for other OAM modes are too weak to identify. As mentioned above, this could be easily understood from the threefold rotational symmetry of the three-leaf clover; see Fig. 1(a).

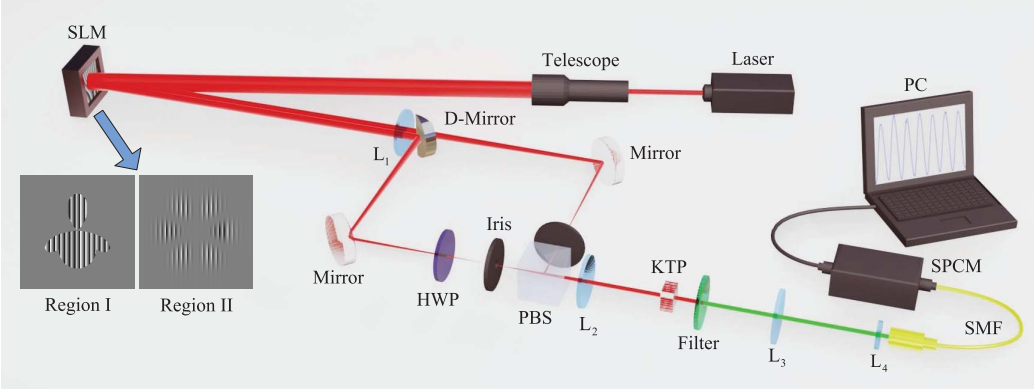

Fig. 2. Experimental setup for upconversion detection of rotational Doppler effect. Insets are the typical holograms displayed in Regions I and II of SLM, respectively.

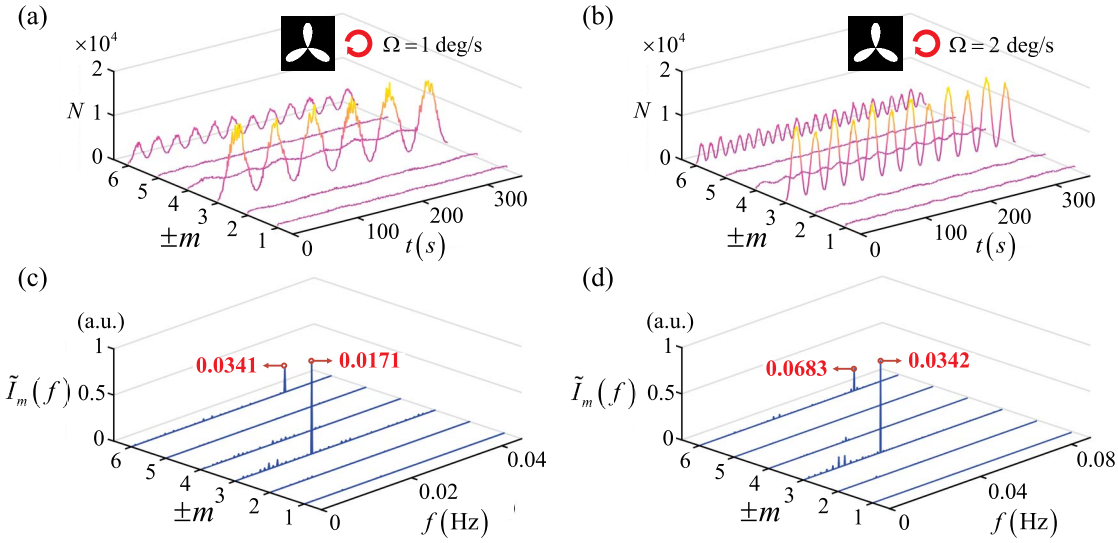

Fig. 3. Experimental results for a rotating clover. (a) and (b) OAM-dependent photon counts (N) of SHG light, where $\Omega = 1$ deg/s and 2 deg/s, respectively. (c) and (d) The corresponding power spectra of rotational Doppler signals after FFT, in which the beat frequencies are marked as well.

Thus, we use the peak power signals in the recorded Doppler spectra to deduce the angular velocities of the rotating clover. For Fig. 3(c), it is observed that $f = 0.0171$ Hz at $m = \pm 3$ and $f = 0.0341$ Hz at $m = \pm 6$. Then, according to the relation $f_{\mathrm{mod}} = m\Omega/\pi$, we have $\Omega = 1.0260$ deg/s and $\Omega = 1.0230$ deg/s, with the relative error both smaller than 2.60%. For Fig. 3(d), we observe $f = 0.0342$ Hz at $m = \pm 3$ and $f = 0.0683$ Hz at $m = \pm 6$. Therefore, we have $\Omega = 2.0520$ deg/s and $\Omega = 2.0490$ deg/s, with the relative errors both smaller than 2.60%.

Without loss of generality, we further consider other objects of more complex structures, such as a snowflake and a cartoon pattern. In our experiment, both patterns are set to rotate at the same constant angular velocity of 4 deg/s. For the snowflake of Figs. 4(a) and 4(c), we can see that the dominant Doppler signals of SHG light appear at the measured OAM superpositions of $m = \pm 6$ and $m = \pm 12$, in which the cosine oscillations of single-photon events can be seen clearly. This is again due to the obvious sixfold rotational symmetry of the snowflake as an echo of Fig. 1(b). We observe that $f = 0.1318$ Hz at $m = \pm 6$ and $f = 0.2637$ Hz at $m = \pm 12$, which give rise to the measured angular velocities of $\Omega = 3.9540$ deg/s and $\Omega = 3.9555$ deg/s, respectively, with the relative errors both smaller than 1.15%. In contrast, for the cartoon pattern that has a relatively low symmetry, we plot the rotational frequency shifts by scanning the OAM superpositions from $m = \pm 1$ to $m = \pm 6$; see Figs. 4(b) and 4(d). We observe the obvious cosine signals for $m = \pm 1$, ± 2, ± 3, and ± 6. As mentioned in Fig. 1(c), these results also manifest the fact that the cartoon pattern contains a variety of LG mode components, as a result from its own structural property of low symmetry. Similarly, we use the peak signals in the power spectra to deduce the angular

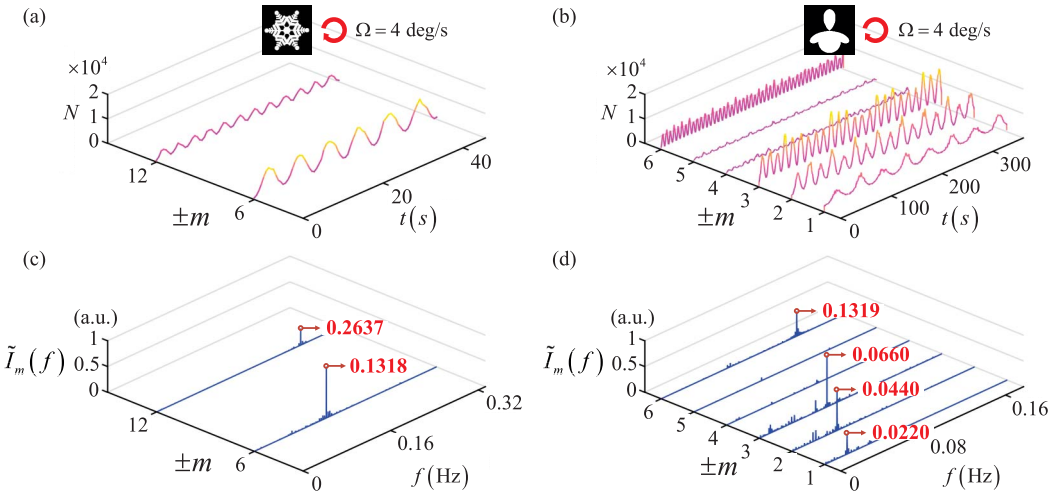

Fig. 4. Experimental results for a rotating snowflake and a cartoon pattern, respectively. (a) and (b) OAM-dependent photon counts (N) of SHG light, where $\Omega = 4$ deg/s for both cases. (c) and (d) The corresponding power spectra of rotational Doppler signals, in which the beat frequencies are marked as well.

velocities of the rotating cartoon pattern. We observe from Fig. 4(d) that $f = 0.0220$ Hz at $m = \pm 1$, $f = 0.0440$ Hz at $m = \pm 2$, $f = 0.0660$ Hz at $m = \pm 3$, and $f = 0.1319$ Hz at $m = \pm 6$, respectively. Therefore, we have $\Omega = (3.9592 \pm 0.0015)$ deg/s, which again confirms the effectiveness of our scheme.

4. CONCLUSION

In conclusion, based on frequency upconversion, we have developed a new scheme for detecting the angular velocities of rotating objects via SHG. We have used one infrared FW to probe a rotating object and amplified the tiny angular velocity by the OAM numbers of the other FW as a result of transferring the rotational frequency shifts from the infrared to the visible region at low photon-count rates. Besides, the measured power spectra of Doppler signals also reflect the geometric symmetry of the rotating objects. Also, the periodically poled crystals, e.g., periodically-poled potassium titanyl phosphate (PPKTP), can be a better candidate to enable strong photon–photon interaction and to realize high-efficiency frequency conversion [39]. Thus, infrared monitoring and remote sensing even at the few-photon level will become more feasible in the future studies.

Funding. Key Research Projects of Foundation Strengthening Program of China (2019-JCJQ-ZD); National Natural Science Foundation of China (12034016); Fundamental Research Funds for the Central Universities at Xiamen University (20720190057, 20720200074); China Postdoctoral Science Foundation (2021M691891); Natural Science Foundation of Fujian Province of China for Distinguished Young Scientists (2015J06002); Program for New Century Excellent Talents in University (NCET-13-0495).

Acknowledgment. The authors thank Dr. Tong Liu from Space Engineering University for helpful technical discussions.

Disclosures. The authors declare no conflicts of interest.

Data Availability. Data underlying the results presented in this paper are not publicly available at this time but may be obtained from the authors upon reasonable request.

REFERENCES

1. C. Doppler, *Über das farbige Licht der Doppelsterne und einigeranderer Gestirne des Himmels* (1842).
2. M. Padgett, "Electromagnetism: like a speeding watch," Nature **443**, 924–925 (2006).
3. B. A. Garetz and S. Arnold, "Variable frequency shifting of circularly polarized laser radiation via a rotating half-wave retardation plate," Opt. Commun. **31**, 1–3 (1979).
4. J. Courtial, K. Dholakia, D. A. Robertson, L. Allen, and M. J. Padgett, "Measurement of the rotational frequency shift imparted to a rotating light beam possessing orbital angular momentum," Phys. Rev. Lett. **80**, 3217–3219 (1998).
5. J. Courtial, D. A. Robertson, K. Dholakia, L. Allen, and M. J. Padgett, "Rotational frequency shift of a light beam," Phys. Rev. Lett. **81**, 4828–4830 (1998).
6. M. P. Lavery, F. C. Speirits, S. M. Barnett, and M. J. Padgett, "Detection of a spinning object using light's orbital angular momentum," Science **341**, 537–540 (2013).
7. L. Marrucci, "Spinning the Doppler effect," Science **341**, 464–465 (2013).
8. S. Barreiro, J. W. R. Tabosa, H. Failache, and A. Lezama, "Spectroscopic observation of the rotational Doppler effect," Phys. Rev. Lett. **97**, 113601 (2006).
9. H. Luo, S. Wen, W. Shu, Z. Tang, Y. Zou, and D. Fan, "Rotational Doppler effect in left-handed materials," Phys. Rev. A **78**, 033805 (2008).
10. O. Korech, U. Steinitz, R. J. Gordon, I. S. Averbukh, and Y. Prior, "Observing molecular spinning via the rotational Doppler effect," Nat. Photonics **7**, 711–714 (2013).
11. H. Zhou, D. Fu, J. Dong, P. Zhang, and X. Zhang, "Theoretical analysis and experimental verification on optical rotational Doppler effect," Opt. Express **24**, 10050–10056 (2016).
12. H. L. Zhou, D. Z. Fu, J. J. Dong, P. Zhang, D. X. Chen, X. L. Cai, F. L. Li, and X. L. Zhang, "Orbital angular momentum complex spectrum analyzer for vortex light based on the rotational Doppler effect," Light Sci. Appl. **6**, e16251 (2017).
13. W. Zhang, J. Gao, D. Zhang, Y. He, T. Xu, R. Fickler, and L. Chen, "Free-space remote sensing of rotation at the photon-counting level," Phys. Rev. Appl. **10**, 044014 (2018).
14. Y. Zhai, S. Fu, C. Yin, H. Zhou, and C. Gao, "Detection of angular acceleration based on optical rotational Doppler effect," Opt. Express **27**, 15518–15527 (2019).
15. S. Qiu, T. Liu, Z. Li, C. Wang, Y. Ren, Q. Shao, and C. Xing, "Influence of lateral misalignment on the optical rotational Doppler effect," Appl. Opt. **58**, 2650–2655 (2019).
16. S. Qiu, T. Liu, Y. Ren, Z. Li, C. Wang, and Q. Shao, "Detection of spinning objects at oblique light incidence using the optical rotational Doppler effect," Opt. Express **27**, 24781–24792 (2019).
17. W. Zhang, D. Zhang, X. Qiu, and L. Chen, "Quantum remote sensing of the angular rotation of structured objects," Phys. Rev. A **100**, 043832 (2019).
18. R. D. Hudson and J. W. Hudson, "The military applications of remote sensing by infrared," Proc. IEEE **63**, 104–128 (1975).
19. A. Barth, "Infrared spectroscopy of proteins," BBA-Bioenergetics **1767**, 1073–1101 (2007).
20. S. Türker-Kaya and C. W. Huck, "A review of mid-infrared and near-infrared imaging: principles, concepts and applications in plant tissue analysis," Molecules **22**, 168 (2017).
21. J. Shi, T. T. Wong, Y. He, L. Li, R. Zhang, C. S. Yung, J. Hwang, K. Maslov, and L. V. Wang, "High-resolution, high-contrast mid-infrared imaging of fresh biological samples with ultraviolet-localized photoacoustic microscopy," Nat. Photonics **13**, 609–615 (2019).
22. Q. Weng, "Thermal infrared remote sensing for urban climate and environmental studies: methods, applications, and trends," ISPRS J. Photogramm. **64**, 335–344 (2009).
23. M. Wang, "Remote sensing of the ocean contributions from ultraviolet to near-infrared using the shortwave infrared bands: simulations," Appl. Opt. **46**, 1535–1547 (2007).
24. M. Wang and W. Shi, "Estimation of ocean contribution at the MODIS near-infrared wavelengths along the east coast of the US: two case studies," Geophys. Res. Lett. **32**, L17708 (2005).
25. M. Mrejen, Y. Erlich, A. Levanon, and H. Suchowski, "Multicolor time-resolved upconversion imaging by adiabatic sum frequency conversion," Laser Photon. Rev. **14**, 2000040 (2020).
26. K. J. Kubarych, M. Joffre, A. Moore, N. Belabas, and D. M. Jonas, "Mid-infrared electric field characterization using a visible charge-coupled-device-based spectrometer," Opt. Lett. **30**, 1228–1230 (2005).
27. M. Vollmer and K.-P. Möllmann, *Infrared Thermal Imaging: Fundamentals, Research and Applications* (Wiley, 2010).
28. B. Klein, E. Plis, M. N. Kutty, N. Gautam, A. Albrecht, S. Myers, and S. Krishna, "Varshni parameters for InAs/GaSb strained layer superlattice infrared photodetectors," J. Phys. D **44**, 075102 (2011).
29. R. H. Hadfield, "Single-photon detectors for optical quantum information applications," Nat. Photonics **3**, 696–705 (2009).

30. H. Dong, H. Pan, Y. Li, E. Wu, and H. Zeng, "Efficient single-photon frequency upconversion at 1.06 μm with ultralow background counts," Appl. Phys. Lett. **93**, 071101 (2008).
31. R. T. Thew, H. Zbinden, and N. Gisin, "Tunable upconversion photon detector," Appl. Phys. Lett. **93**, 071104 (2008).
32. C. Pedersen, E. Karamehmedović, J. S. Dam, and P. Tidemand-Lichtenberg, "Enhanced 2D-image upconversion using solid-state lasers," Opt. Express **17**, 20885–20890 (2009).
33. K. Huang, X. Gu, H. Pan, E. Wu, and H. Zeng, "Few-photon-level two-dimensional infrared imaging by coincidence frequency upconversion," Appl. Phys. Lett. **100**, 151102 (2012).
34. K. F. Li, J. H. Deng, X. Liu, and G. Li, "Observation of rotational Doppler effect in second harmonic generation in reflection mode," Laser Photon. Rev. **12**, 1700204 (2018).
35. G. Li, T. Zentgraf, and S. Zhang, "Rotational Doppler effect in nonlinear optics," Nat. Phys. **12**, 736–740 (2016).
36. L. Torner, J. P. Torres, and S. Carrasco, "Digital spiral imaging," Opt. Express **13**, 873–881 (2005).
37. R. W. Boyd and B. R. Masters, *Nonlinear Optics*, 3rd ed. (Academic, 2008).
38. F. Bouchard, N. H. Valencia, F. Brandt, R. Fickler, M. Huber, and M. Malik, "Measuring azimuthal and radial modes of photons," Opt. Express **26**, 31925–31941 (2018).
39. R. Tang, X. Li, W. Wu, H. Pan, H. Zeng, and E. Wu, "High efficiency frequency upconversion of photons carrying orbital angular momentum for a quantum information interface," Opt. Express **23**, 9796–9802 (2015).